Check for updates

View Article Online
View Journal | View Issue

Development of a UPLC-MS/MS method for pesticide analysis in paddy water and evaluation of anodic TiO$_2$ nanostructured films for pesticide photodegradation and antimicrobial applications†

Phuoc Huu Le, [ab] Thao Phuong Huynh, [c] Teng-Ping Chu, [ab] Loc Tan Nguy, [d] Ngo Ngoc Uyen[e] and Tho Chau Minh Vinh Do [*d]

Pesticide contamination in agricultural water poses serious environmental and public health risks, particularly due to the accumulation of harmful residues that threaten aquatic ecosystems and human health. This study investigated the levels of five pesticides—carbaryl (CBR), methiocarb (MTC), diazinon (DZN), chlorpyrifos (CLO), and cypermethrin (CYPER)—in agricultural water samples from Can Tho City and Hau Giang Province, Vietnam. Ultra-performance liquid chromatography-tandem mass spectrometry (UPLC-MS/MS) was employed for their detection and quantification. Chlorpyrifos was the most frequently detected pesticide (32.5%), with concentrations ranging from 1.7 to 10.9 ng mL^{-1}. The concentrations of cypermethrin, carbaryl, methiocarb, and diazinon were 2.6–9.4 ng mL^{-1}, 1.3–14.3 ng mL^{-1}, 4.1–7.7 ng mL^{-1}, and 2.8–10.5 ng mL^{-1}, respectively. The persistence of pesticide residues in the water samples highlights the significant contamination concerns in the region. To address this issue, two types of TiO$_2$ nanophotocatalysts—TiO$_2$ nanotube arrays (TNAs) and TiO$_2$ nanowires on nanotube arrays (TNWs/TNAs)—were synthesized for the photocatalytic degradation of the identified pesticides. Under UV-vis irradiation (~96 mW cm^{-2}), both nanostructures achieved rapid pesticide degradation, with removal efficiencies of up to 99% within 25 minutes. TNWs/TNAs exhibited superior photocatalytic performance, attributed to their increased surface area compared to TNAs. In addition to pesticide degradation, their antibacterial activity was assessed. Under weak UV-vis light (6.3 mW cm^{-2}), both TNAs and TNWs/TNAs achieved 100% antibacterial efficacy against *Escherichia coli*, significantly higher than the 68% efficacy of UV light treatment alone. Even under dark conditions, TNWs/TNAs demonstrated enhanced antibacterial activity, achieving 63% efficacy compared to 12% for TNAs. These results underscore the dual functionality of TNWs/TNAs as effective photocatalysts for both pesticide degradation and bacterial inactivation, presenting a promising approach for agricultural water treatment.

1. Introduction

Pesticides are crucial for agriculture and are used in large quantities in many countries.[1] In Vietnam, the majority of pesticides are imported for use. More than half of the imported

^{a}Center for Plasma and Thin Film Technologies, Ming Chi University of Technology, New Taipei City 243303, Taiwan

^{b}International PhD Program in Plasma and Thin Film Technology, Ming Chi University of Technology, New Taipei City 243303, Taiwan

^{c}Faculty of Pharmacy, Nam Can Tho University, 168 Nguyen Van Cu (Ext) Street, Can Tho City 94000, Vietnam

^{d}Faculty of Pharmacy, Can Tho University of Medicine and Pharmacy, 179 Nguyen Van Cu Street, Can Tho City 94000, Vietnam. E-mail: dcmvtho@ctump.edu.vn

^{e}Faculty of Basic Sciences, Can Tho University of Medicine and Pharmacy, 179 Nguyen Van Cu Street, Can Tho City 94000, Vietnam

† Electronic supplementary information (ESI) available. See DOI: https://doi.org/10.1039/d4na00997e

pesticides are used in the Mekong Delta region (also known as the South-western region) with an area of approximately 39 000 km^2 and a population of approximately 17 million people.[2] Half of the pesticides belong to groups II and III (moderate and mild toxicity) according to the WHO classification.[3] The inappropriate usage and storage of pesticides by people contribute to the high proportion of pesticide contamination in canals, polluting the surface water, which leads to the risk of drug exposure through the drinking route, and causes adverse effects on aquatic life.[3,4] Previous studies in Vietnam have found that residues of active pesticides in water and sediments exist in relatively high concentrations.[3,4] According to V. T. Pham *et al.* (2013), the average concentration of 15 commonly used pesticides in surface water was at a high concentration of 3.34 μg L^{-1}, while the highest concentration belonged to isoprothiolane (11.24 μg L^{-1}).[3] Most analysed water samples had residues of pesticides, namely isoprothiolane, fenobucarb, and fipronil

with maximum concentrations of 8.49 μg L^{-1}, 8.49 μg L^{-1}, and 0.41 μg L^{-1}, respectively.[4] Despite the differences in location and detected frequency–concentration, pesticide contamination has been ubiquitous in the Mekong Delta region, Vietnam. Several types of pesticides were found in various sources of water, including groundwater, surface water, and drinking water.[5–8] The popular detected pesticides included organochlorines (*e.g.*, aldehyde, endosulfan, heptachlor, aldrin, dieldrin, endrin ketone, and heptachlor epoxide) and organophosphates (*e.g.*, parathion-methyl, parathion, and malathion).[7] The detected pesticide levels in some water sources exceeded the permissible limits set by the European Commission, with concentrations reaching as high as 1.38 μg L^{-1} for up to 12 different pesticides in bottled water.[4] Since the Mekong Delta is a major agricultural production area relying on its river and canal system as the primary water supply, it is essential to investigate the current levels of pesticide residues in the waters surrounding key rice-growing regions.

Quantifying pesticides accurately at low concentrations in agriculture-related water samples is challenging due to the complexity of the matrix. The analysis of pesticide residues in water primarily relies on chromatographic techniques, notably gas chromatography (GC) and liquid chromatography (LC), often coupled with mass spectrometry (MS). Among these, LC-MS has gained prominence due to its versatility in detecting a broad range of chemical classes, including poorly volatile compounds. GC-MS and LC-MS/MS are widely used for their exceptional sensitivity and selectivity, frequently achieving detection limits below ng L^{-1}—essential for complying with stringent regulatory standards set by organizations such as the EU and the Codex Alimentarius Commission.[9,10] While methods such as liquid chromatography- or gas chromatography-tandem mass spectrometry (LC-MS/MS or GC-MS/MS) have been developed for analysing pesticide multi-residues in aquatic environments of drinking water, surface water, and wastewater effluents,[11,12] only a few studies have been conducted on analysing pesticide residues in agriculture-related wastewater and river- and canal-water samples from the Vietnamese Mekong Delta. UPLC-MS/MS offers high sensitivity for studying the occurrence and fate of pesticides in the environment; however, it remains a significant challenge to analysing pesticides with multiple classes and a complex matrix, which calls for a systematic study to develop a robust UPLC-MS/MS method for addressing these complexities.

Effective treatment of emerging contaminants, such as pesticides and pharmaceuticals, in aqueous environments is a growing concern. Conventional wastewater treatment plants are inadequate for removing these contaminants, which are often chemically stable;[6,13] meanwhile, advanced oxidation processes (AOPs) have recognized as a promising solution for treating water pollutants with high chemical stability.[14] Semiconductor photocatalysis has been demonstrated as an effective technology for decontaminating pesticides and other emerging pollutants.[15] The working principle of AOPs is associated with the generation of electrons and holes under UV/vis irradiation, which in turn create highly reactive ˙OH and O$_2$˙$^{-}$ to degrade different pollutants in treated water.

Titanium dioxide (TiO$_2$) nanomaterials are widely used for photocatalytic degradation of organic-, pharmaceutical-, and pesticide pollutants/contaminants in aqueous environments because of their excellent activity, stability, nontoxicity, low cost, and a large surface area.[16–18] Among various nanostructures, we are interested in studying the TiO$_2$ nanotube arrays (TNAs) and TiO$_2$ nanowires on nanotube arrays (TNWs/TNAs) owing to their unidirectional electrical channel and the large surface-to-volume ratio.[19–21] TiO$_2$ nanotube arrays, typically synthesized *via* anodization, feature highly ordered, porous structures with elongated channels, significantly increasing the surface area for pollutant adsorption and promoting efficient charge separation in photocatalytic reactions. Similarly, TiO$_2$ nanowires grown on nanotube arrays through anodization form a modified 1D nanostructured film, further enhancing the photocatalytic activity in the degradation of methylene blue and anticancer drugs.[20,22,23] These TiO$_2$ nanostructures play a crucial role in contaminant degradation by improving pollutant–TiO$_2$ interactions and enhancing the generation of reactive oxygen species, such as hydroxyl radicals (˙OH) and superoxide anions (O$_2$˙$^{-}$). Additionally, both TNAs and TNWs/TNAs are synthesized on immobilized titanium foil through a simple anodic oxidation process, allowing for easy retrieval of the nanophotocatalysts from the treated solution after use and enabling their reuse multiple times. The reusability of TiO$_2$ materials has been widely demonstrated in previous studies,[22,24–27] showing their ability to maintain high photocatalytic performance over multiple cycles. TiO$_2$-based nanostructured films hold great promise for sustainable environmental applications.

While the photocatalytic degradation of methylene blue and antibiotics using TNAs and/or TNWs/TNAs has been extensively studied,[20,21,23,28] their potential for breaking down pesticide residues in aqueous environments remains largely unexplored. Given the widespread contamination of water sources with pesticides, assessing the effectiveness of TNAs and TNWs/TNAs in this context is essential. According to a review article, titanium dioxide nanoparticles have been extensively used to degrade 53 individual active ingredients and one pesticide mixture.[29] Among these, organophosphorus compounds accounted for the largest share (22%), followed by triazine derivatives (11%), chloropyridines (9%), and organochlorines (9%).[29] However, the average photodegradation efficiency was limited to 71%,[29] underscoring the need for more effective photocatalytic materials. Investigating TNAs and TNWs/TNAs for pesticide degradation could offer a promising strategy to enhance the photocatalytic performance for water purification.

TiO$_2$ has gained considerable attention for its strong antimicrobial properties, particularly in eliminating harmful bacteria like *Escherichia coli* (*E. coli*) through photocatalysis.[30,31] Upon exposure to ultraviolet (UV) light, TiO$_2$ produces reactive oxygen species (ROS) such as hydroxyl radicals and superoxide anions, which cause oxidative damage to bacterial cell walls, leading to cell death.[32–34] *E. coli* is often used as a model organism in antimicrobial research due to its well-studied biology, its relevance as a common pathogen in contaminated environments, and its robust outer membrane, which poses

a significant challenge to antimicrobial agents. The antimicrobial activity of nanoparticles, including TiO_2, is influenced by factors such as morphology, size, chemical composition, and nanostructure.[35,36] For TiO_2 nanoparticles, their antimicrobial effectiveness is closely tied to their photocatalytic performance, which depends on their morphological and structural properties.[37] Among TiO_2's crystal phases, anatase exhibits the highest photocatalytic and antimicrobial activity.[38] While the bactericidal properties of TiO_2 in various forms, such as nanoparticles and thin films, are well-documented,[39-41] the specific antimicrobial efficacy of TNAs and TNWs/TNAs against *E. coli* remains largely unexplored. Thus, research is needed to assess their potential as highly efficient antimicrobial materials.

In this study, we developed a robust UPLC-MS/MS method to detect five commonly used pesticides in rice agriculture that pose significant risks to human health and the environment. The targeted pesticides include the organophosphates diazinon and chlorpyrifos, the carbamates carbaryl and methiocarb, and the pyrethroid cypermethrin. This method was applied to analyze 40 water samples collected from rivers and canals near rice farming areas in Can Tho City and Hau Giang Province in the Vietnamese Mekong Delta. Additionally, the UPLC-MS/MS method was used to study the photocatalytic degradation kinetics of these pesticide residues in selected water samples, utilizing TNAs and TNWs/TNAs as photocatalysts. A comprehensive characterization of the TNAs and TNWs/TNAs was conducted, examining their structural, morphological, compositional, optical, and bactericidal properties. This study promotes both pesticide detection methodologies and the development of TiO_2-based nanophotocatalysts for pesticide degradation and antimicrobial applications.

2. Materials and methods

2.1. Chemicals and reagents

The external standards (carbaryl, methiocarb, diazinon, chlorpyrifos, and cypermethrin) and the internal standard (triphenylphosphate) were obtained from Sigma-Aldrich (USA). Disodium ethylenediaminetetraacetate (Na_2EDTA) was sourced from Merck. High-purity acetonitrile and methanol were provided by JT Baker, while water and formic acid were supplied by Merck. Ultra-pure water from a Milli-Q® ultra-pure water system was used. Stock solutions with a concentration of 1 mg mL^{-1} were prepared in methanol and stored at 5 °C. Working solutions of all pesticide standard mixtures were prepared by appropriately diluting the corresponding stock solutions.

2.2. Sample collection

Water samples were collected from the inland and main canals of rice-growing areas in Can Tho City and Hau Giang Province, located in the Vietnamese Mekong Delta. The collection included ten agricultural wastewater samples from Thot Not district (CT-TN-10) and ten from Thoi Lai district (CT-TL-10) in Can Tho City, along with ten wastewater samples from Chau Thanh district (HG-CT-10) and ten from Nga Bay City (HG-NB-

10) in Hau Giang Province. The sampling locations are shown in Fig. S1.†

2.3. Sample pre-treatment

Water samples were collected and stored in amber glass bottles, pre-rinsed with ultra-pure water, and used within 12 hours. The samples were then filtered through a Whatman 1-µm glass fiber filter, followed by a 0.45-µm nylon membrane filter. A sample without any target compound was used as a blank. Two extraction procedures were carried out to maximize the recovery of target compounds by spiking a blank sample with a mixture of analyte standards.

In the first procedure, Strata C18-E (500 mg) solid-phase extraction (SPE) cartridges from Phenomenex were used. The cartridges were conditioned with 5 mL of methanol, followed by 5 mL of Milli-Q water, each at a flow rate of 1 mL min^{-1}. The water sample (5 mL) was passed through the SPE cartridges at 3 mL min^{-1} *via* a 12-port vacuum manifold (Phenomenex, USA). Subsequently, the cartridges were rinsed with 5 mL of a solution containing 5% methanol and 95% Milli-Q water, maintaining the same flow rate (3 mL min^{-1}), to eliminate any potential interfering compounds. After vacuum drying the cartridges for 5 minutes, elution was performed using 5 mL of ethyl acetate at a flow rate of 1 mL min^{-1}. The eluates were dried with anhydrous Na_2SO_4 (500 mg) to remove any residual water. Blank samples were also processed to check for any carryover during the SPE process. The eluates were evaporated under a gentle nitrogen stream and reconstituted with 5 mL of acetonitrile–water (50 : 50, v/v) for further UPLC-MS/MS analysis. In the second procedure, the sample pH was adjusted to 2.5 using 0.1 M HCl. To enhance complex formation with inorganic compounds in the matrices, 1 mL of 5% (w/v) Na_2EDTA was added to a 50 mL homogenized blank sample.

2.4. UPLC-MS/MS analysis

UPLC-MS/MS analysis was performed using an Acquity UPLC H-Class system (Waters Corporation, Milford, USA) connected to a Xevo TQD mass spectrometer. The instrument featured an electrospray ionization (ESI) source and was operated in multiple reaction monitoring (MRM) mode. High-purity nitrogen (99.9%) served as the desolvation gas, and argon was employed to induce dissociation during MS/MS analysis. Positive ion mode was utilized with a capillary voltage set to 4.5 kV, a source temperature of 150 °C, and a desolvation temperature of 500 °C. A nitrogen sheath gas flow rate of 1000 L h^{-1} was maintained throughout the process.

To ensure optimal and stable signals for both precursor and fragment ions, direct infusion of each compound's standard solution (200 ng mL^{-1}) was conducted. MassLynx 4.1 software, along with the IntelliStart tool, was used for data acquisition and optimization of MS/MS parameters such as cone voltage and collision energy. Compound-specific tune files were generated for each standard under continuous flow conditions to optimize key parameters (cone voltage, collision energy, and fragment ions). Direct injection into the ionization chamber, coupled with LC, was employed during the scanning process.

The stationary phase of a chromatographic column plays a critical role in determining the separation efficiency in chemical separation processes. In this study, three analytical columns were evaluated: a Phenomenex Lunar C8 column (3 μm, 150 × 4.6 mm), an Eclipse Plus C18 column (3.5 μm, 150 × 4.6 mm), and a Kinetex Phenyl-hexyl column (1.7 μm, 50 × 2.1 mm). Several sample diluents were also tested, including 0.1% formic acid in water, a methanol–water mixture with 0.1% formic acid (50 : 50, v/v), and a 50 : 50 (v/v) acetonitrile–water blend. To optimize the mobile phase, methanol–water mixtures with varying concentrations of formic acid (0.01% to 0.15%) were explored. The injection volume was set at 10 μL, and separation was conducted at 25 °C using a gradient mobile phase comprising methanol (A) and water with formic acid (B).

2.5. Method validation

Matrix effects were evaluated by comparing the slope ratios of matrix-matched calibration curves to standard solution calibration curves. The percentage slope ratio indicated signal suppression (positive values) or enhancement (negative values). Method optimization was validated based on specificity, sensitivity, linearity, precision, and accuracy. Specificity was confirmed according to the EU Regulation 2021/808, with LC providing one identification point and two MRM transitions providing a total of four identification points.

During UPLC-MS/MS analysis, co-elution of compounds within the chromatographic system can lead to ion suppression or enhancement due to ionization competition, especially in complex matrices. To address matrix effects, calibration curves were generated using matrix-matched solutions prepared by spiking analytes into wastewater extracts at seven concentrations ranging from the lowest detectable limit to 250 ng mL^{-1}. Each concentration was injected three times, and peak areas were integrated. Triphenylphosphate (TPP) was used as the internal standard in this analysis. The method detection limit (MDL) and method quantitation limit (MQL) were defined as the concentrations at which chromatographic peaks were three and ten times higher than the baseline noise, respectively.

To evaluate extraction recoveries, blank agricultural wastewater samples were spiked with reference compounds at three concentration levels, with six replicates each for untreated and treated wastewater samples. Recovery rates were calculated by comparing experimental results with theoretical values, and relative standard deviations (RSDs) were determined to assess the reproducibility. Intermediate precision was measured by analyzing one sample six times in quintuplicate on the first day and repeating the process over two additional days to calculate intra-day and inter-day precision.

2.6. Synthesis of TiO$_2$ nanotube arrays (TNAs) and TiO$_2$ nanowires on TiO$_2$ nanotube arrays (TNWs/TNAs)

TNAs and TNWs/TNAs were synthesized on titanium foil substrates (99% purity; dimensions: 12 mm × 24 mm × 0.5 mm) via anodization. The titanium substrates were pre-cleaned through sonication in acetone, methanol, and deionized water, with each solvent applied for 10 minutes. Anodization was performed in a two-electrode configuration, utilizing the titanium substrate as the anode and a stainless steel sheet as the cathode. The electrolyte was formulated with 0.3% by weight NH$_4$F dissolved in ethylene glycol, supplemented with 5% by volume deionized water. TNA and TNW/TNA films were anodized at a constant voltage of 30 V for 1.5 hours and 3 hours, respectively. After anodization, the samples were thermally treated in an air atmosphere at 400 °C for 2 hours to promote crystallization.

The synthesized TiO$_2$ nanomaterials were characterized structurally and compositionally using X-ray diffraction (XRD; Bruker D2) with Cu Kα radiation ($\lambda = 1.5406$ Å) in a $2\theta-\theta$ configuration to analyze the crystal structure. The surface morphology and film thickness were evaluated via field-emission scanning electron microscopy (FE-SEM; JEOL JSM-6500), while elemental composition was determined using an energy-dispersive X-ray (EDS) spectrometer (Oxford) integrated into the FE-SEM system. EDS spectroscopy analyses were performed at an accelerating voltage of 15 kV, with a dead time of 20–30% and a 60-second data acquisition period. Structural characterization at the atomic scale was performed using high-resolution scanning transmission electron microscopy (HRTEM, JEOL JEM-ARM200F) operating at 200 kV. Specimens for TEM analysis were prepared by mechanically exfoliating the film surface with a diamond tip and depositing the fragments onto a copper grid.

For surface composition and chemical state analysis, X-ray photoelectron spectroscopy (XPS, ESCALAB Xi+, Thermo Fisher Scientific) equipped with an Al Kα X-ray source (1486.6 eV) was employed to study TNAs and TNWs/TNAs. Binding energies were referenced to the C 1s peak at 284.6 eV for calibration. Spectral deconvolution of the XPS data was conducted using XPSPEAK 4.1 software, incorporating Shirley background correction and Gaussian–Lorentzian peak fitting. The optical properties and band gaps of the TiO$_2$ nanostructured films were examined by diffuse reflectance spectroscopy (DRS) performed using a JASCO V-670 UV-vis-NIR spectrophotometer, with measurements taken across a wavelength range of 200 to 1200 nm at a scan speed of 100 nm min^{-1}. The Raman spectra of TNAs and TNWs/TNAs were recorded using a Renishaw inVia confocal spectrometer under red laser (633 nm Renishaw RL633 HeNe) excitation.

For photocatalytic experiments, TiO$_2$ films were immersed in 30 mL of pesticide solution derived from selected environmental samples. The reaction was conducted under UV-vis illumination ($\sim$96 mW cm^{-2}) provided by a 100 W xenon lamp. Before exposure to light, the TiO$_2$ films were kept in the pesticide solution for 20 minutes in the dark to reach absorption–desorption equilibrium. During photocatalytic reactions, the temperature was maintained between 31 °C and 33 °C. At specified intervals (0 to 25 minutes), treated pesticide samples were collected for quantitative analysis using UPLC-MS/MS.

The bacterial viability assay was conducted using *Escherichia coli* (ATCC 25922) as the test strain. *E. coli* was cultured in nutrient broth at 37 °C for 22 hours to achieve a concentration of 1×10^8 CFU mL^{-1}, with cell growth monitored at 600 nm (OD$_{600}$) to reach an optical density of approximately 0.6. The

culture was then prepared in Luria Bertani (LB) broth (BioShop Canada Inc.) and serially diluted to a final concentration of 1×10^4 CFU mL^{-1}. Subsequently, 0.1 mL of the bacterial suspension was applied to a 1.2 cm × 2.0 cm area on each sample. The TNA and TNW/TNA samples were placed in sterilized Petri dishes, and 100 μL of *E. coli* suspension was carefully deposited on the surface of each sample. The dishes were either kept in the dark or exposed to UV light (wavelength: 253 nm, 32 W, 6.3 mW cm^{-2}) for 10 minutes, then washed and incubated at 37 °C for 22 hours. Colony counting was performed to determine the number of viable bacteria (CFU mL^{-1}), thus evaluating bacterial viability.

3. Results and discussion

3.1. UPLC-MS/MS analysis

The performance of the quadrupole triple mass spectrometer was optimized to achieve the maximum signal intensity for the targeted compounds. In positive ion mode, the ionization of analytes was enhanced, with most pesticides monitored using MRM transitions, which involved the precursor ion and the two most abundant fragment ions. The observed fragment ions for pesticides CBR, MTC, DZN, CLO, and CYPER were consistent with data from the MassBank Europe, MassBank of North America, and previous studies.[42,43]

Optimizing the desolvation temperature and gas flow rates significantly improved the signal intensity. The desolvation temperature of 500 °C was identified as optimal, as lower temperatures resulted in incomplete evaporation of the mobile phase, causing signal reduction. Similarly, increasing the source gas flow rate enhanced the intensity of fragment ion signals, with a maximum observed at 850–1000 L h^{-1}. The selected evaporator gas flow rate was 1000 L h^{-1}.

The choice of solvent for sample dissolution had a notable impact on the ionization efficiency. The ACN : water (50 : 50) solvent composition effectively dissolved the analytes, amplifying the signal strength of both the parent ion [MH]$^+$ and the fragment ions. This optimization ensured robust sensitivity and accuracy for the detection of the targeted pesticides. These findings demonstrate the importance of fine-tuning parameters, including temperature, gas flow rates, and solvent composition, to achieve reliable and sensitive mass spectrometric analysis. Key experimental parameters are summarized in Table S1.†

Among the tested columns, the Kinetex Phenyl-hexyl column demonstrated superior performance in separating pesticides with medium polarity, exhibiting enhanced separation, improved peak shape, and stronger signal intensity. This performance is attributed to the compatibility of the phenyl-hexyl moieties within the column for analytes of this nature. Additionally, the core–shell packed particles of the Kinetex column significantly contributed to its high separation efficiency, with the smaller particle size further enhancing this effect.

Regarding sample diluents, the acetonitrile–water (50 : 50) formulation provided the most favorable peak shape and was the most practical one for sample preparation, requiring only
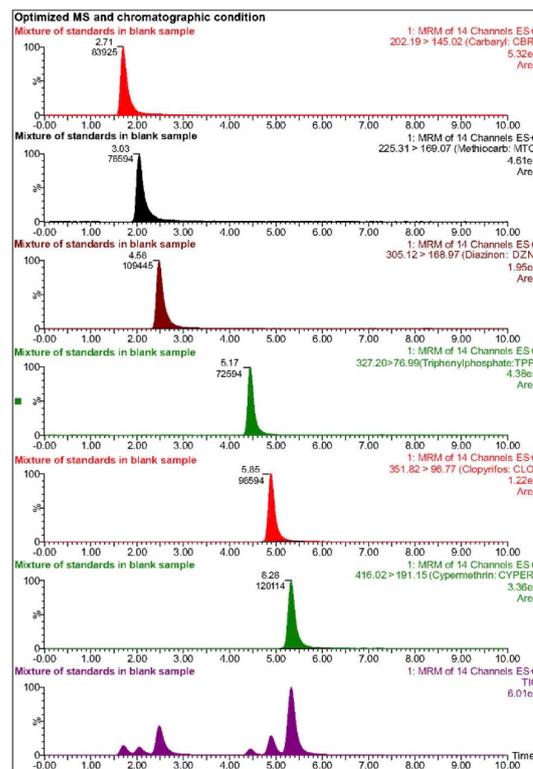

Fig. 1 Chromatographic separation of standard pesticides in untreated wastewater samples.

a simple 1 : 1 dilution with acetonitrile before injection. The optimization of the mobile phase revealed that a 0.12% formic acid concentration (pH = 2.15) yielded enhanced separation, improved peak shape, and higher signal intensity for the pesticides.

The optimal chromatographic conditions for pesticide analysis were achieved using the Kinetex Phenyl-hexyl column (1.7 μm, 50 × 2.1 mm), an acetonitrile–water (50 : 50) sample diluent, and a ternary gradient mobile phase. Analyte elution occurred at approximately 6.5 minutes, with a total analysis time of 10 minutes, including 3.5 minutes for mobile phase re-equilibration. Table S2† provides detailed optimized chromatographic conditions, and Fig. 1 illustrates the separation performance.

3.2. Sample preparation

Based on our experiments and a review of previous studies,[44–47] the optimal sample processing procedure was established as follows:

(1) The sample is initially filtered twice through a 1-μm paper filter (90 mm) to remove any large impurities. Following this, the sample is acidified by adding 0.1% formic acid, and then a 5% Na$_2$EDTA solution is introduced to chelate and eliminate any metal residues. The sample is then filtered through a 0.22-μm membrane filter to remove any remaining impurities before proceeding to analysis.

(2) The analytical sample is further acidified to a pH of 2.5, closely matching the pH of the aqueous mobile phase

containing 0.1% formic acid. At this pH, the analytes are well-solubilized and exist in forms that enhance the accuracy of the analysis while efficiently removing less polar organic impurities. It is important to note that the presence of impurities can interfere with the analysis and compromise the results.

(3) Incorporating 5% Na$_2$EDTA in the sample preparation process significantly improves the recovery efficiency for two key reasons. First, the simplified process involves fewer steps, reducing the potential error. Second, Na$_2$EDTA effectively removes heavy metal ion residues, which are problematic for mass spectrometry due to interference from the instrument's magnetic field. The use of Na$_2$EDTA greatly reduces the background noise during analysis. Experimental results indicate that the recovery rate of the EDTA-based process (Process 2) is superior to that of the SPE-based process (Process 1). Additionally, Process 2 demonstrates faster sample processing (5 minutes) and stronger signal intensity (12.5×10^6) compared to Process 1, which requires 60 minutes and produces a signal intensity of 6.44×10^6 (Table S3†). These findings highlight the effectiveness of EDTA in the sample processing stage, resulting in reduced analysis time and lower overall costs.

3.3. Method validation

Matrix effects are significant for most pesticides, with deviations exceeding the 20% threshold set by EC-2021, rendering pure standard solution calibration curves unreliable for quantitative analysis. By using matrix-matched calibration curves with TPP as the internal standard, the matrix effects were effectively accounted for, allowing accurate quantification of pesticides in complex wastewater samples. The calibration curves demonstrated excellent linearity, with r^2 values of 0.995 or higher, across a broad dynamic range of values of 0.1–250 ng mL^{-1}.

Sensitivity, expressed as MDLs and MQLs, ranged from 0.001 to 0.125 ng mL^{-1} and from 0.05 to 0.30 ng mL^{-1}, respectively, meeting the expected values for triple quadrupole mass spectrometry. Recovery experiments across three concentration levels within the dynamic range showed recovery rates between 85.54% and 104.67%, confirming the high accuracy of the sample preparation process. The relative standard deviation (RSD) for all pesticides remained below 6.32%, well within the 15% threshold, indicating strong precision.

The selectivity of the method was further demonstrated by the retention time RSDs for all pesticides, which were below 0.4%, far below the 2.5% tolerance. Additionally, the relative intensity difference between the two MRM transitions was below 20%, confirming compliance with the EU guidelines for pesticide confirmation. Selectivity was validated by ensuring no interference from blank matrices at the retention times of the analytes or internal standards. The detailed results are summarized in Table S4.†

3.4. Assessment of residual pesticides in agricultural wastewater samples

The presence of pesticide residues in agricultural wastewater poses a significant environmental concern in the Mekong Delta region of Vietnam. This study assessed 40 agricultural wastewater samples collected from inland canals in rice-growing areas of Can Tho City and Hau Giang Province, Vietnam. The results revealed that 13 out of the 40 canal water samples contained pesticide residues at varying concentrations, including CBR, MTC, DZN, CLO, and CYPER. As shown in Table S5,† CLO was the most frequently detected pesticide, present in 13 out of 40 samples (32.5%) at concentrations ranging from 1.7 to 10.9 ng mL^{-1}. Residues of MTC were found in 6 samples (15%), CBR in 8 samples (20%), DZN in 5 samples (12.5%), and CYPER in 7 samples (17.5%). Notably, one sample from CT-TN3 contained exceptionally high concentrations of DZN and CBR, 10.5 ng mL^{-1} and 14.3 ng mL^{-1}, respectively. The detection of pesticide residues in these samples underscores the widespread contamination, posing substantial environmental risks. These findings provide crucial insights into the extent of pesticide pollution in the canals of agriculturally intensive areas of Mekong Delta, Vietnam. Table S6† offers a comprehensive comparison between the results of this study and prior research, emphasizing notable differences and advancements in the analysis of pesticide residues within agricultural and aquatic ecosystems.

3.5. Structural, morphological, optical and compositional properties of TiO$_2$ nanomaterials

Fig. 2 shows the XRD patterns of TNAs and TNWs/TNAs. Both samples exhibited the anatase phase of TiO$_2$, with preferred orientations along the (101) and (112) planes (JCPDS No. 21-1272). The grain sizes (D) of TNAs and TNWs/TNAs were calculated using the Scherrer equation: $D = 0.9\lambda/\beta \cos \theta$, where $\lambda = 1.5406$ Å (the X-ray wavelength for Cu Kα radiation), and β and θ represent the full width at half-maximum and the Bragg diffraction angle of the TiO$_2$ (004) peak, respectively.[20] The calculated grain sizes for TNAs and TNWs/TNAs were nearly identical (31.33 nm $vs.$ 31.03 nm), suggesting similar grain size and crystallinity.

Fig. 3 presents SEM images and EDS spectra of TNAs and TNWs/TNAs. In Fig. 3(a), the TNAs exhibit a well-defined nanotube array structure with an average nanotube diameter of approximately 100 nm and a film thickness of around 3.53 μm (Fig. 3(a)). Meanwhile, TNWs/TNAs present ~1.5 μm-length
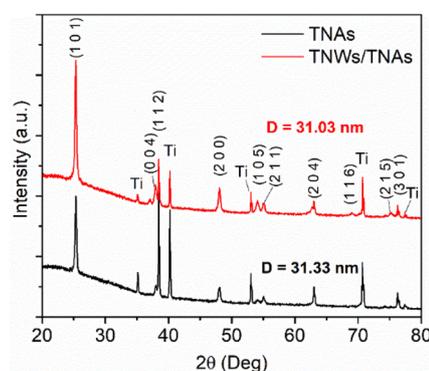

Fig. 2 XRD patterns of TNAs and TNWs/TNAs, with grain size (D) calculated using the Scherrer equation as shown in the figure.
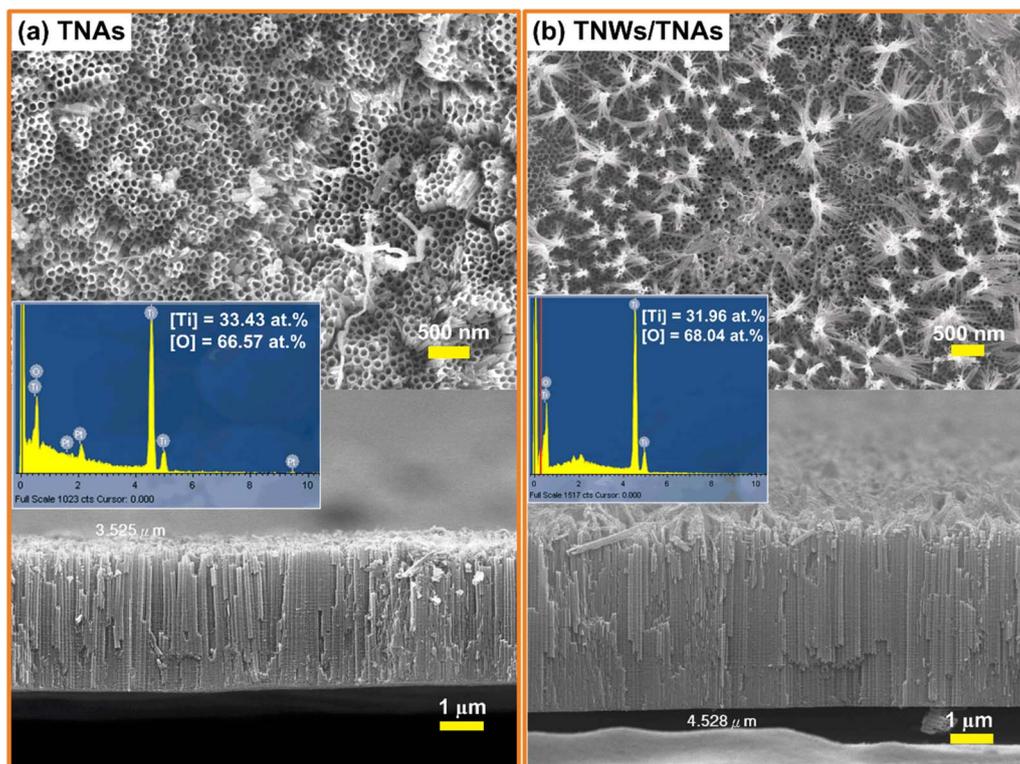
Fig. 3 SEM top-view and cross-sectional images of (a) TNAs and (b) TNWs/TNAs. The lower insets display the EDS spectra of the respective samples, with the atomic percentages of Ti and O indicated in the spectra.

TiO$_2$ nanowires partially covering the TNAs, and they had a film thickness of approximately 4.53 μm. The thicker film of TNWs/TNAs compared to the TNA film is due to the longer anodizing time (3 h *vs.* 1.5 h). The insets in Fig. 3 show the EDS spectra of TNAs and TNWs/TNAs; both had very similar EDS spectra with the presence of Ti, O, and Pt peaks. Noticeably, Pt peaks were observed due to the Pt coating for the SEM measurement that requires a good conductive sample. In addition, the EDS analysis confirmed that both films possessed close stoichiometry of TiO$_2$ (*i.e.*, [Ti] = 33.43 at% and [O] = 66.57 at% for TNAs; [Ti] = 31.96 at% and [O] = 68.04 at% for TNWs/TNAs). The
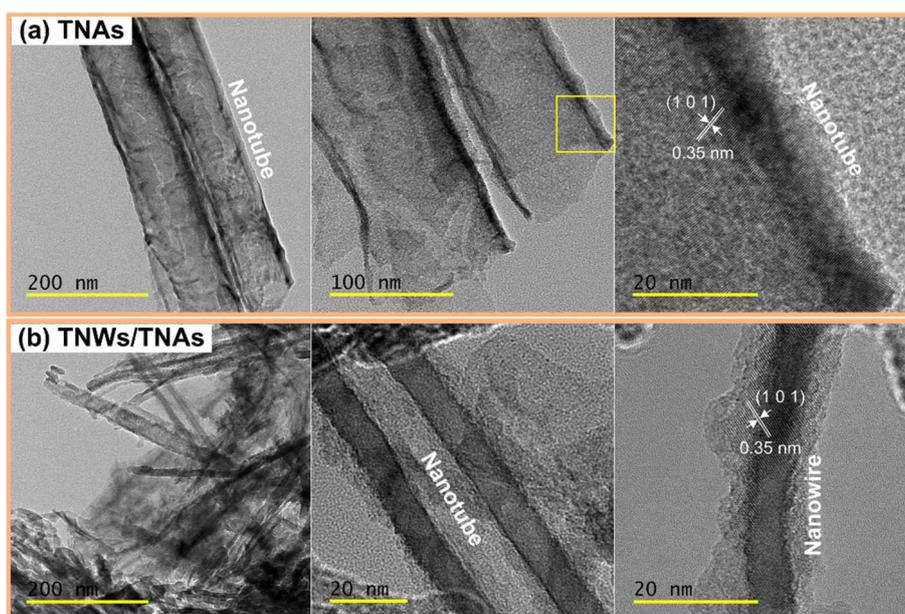

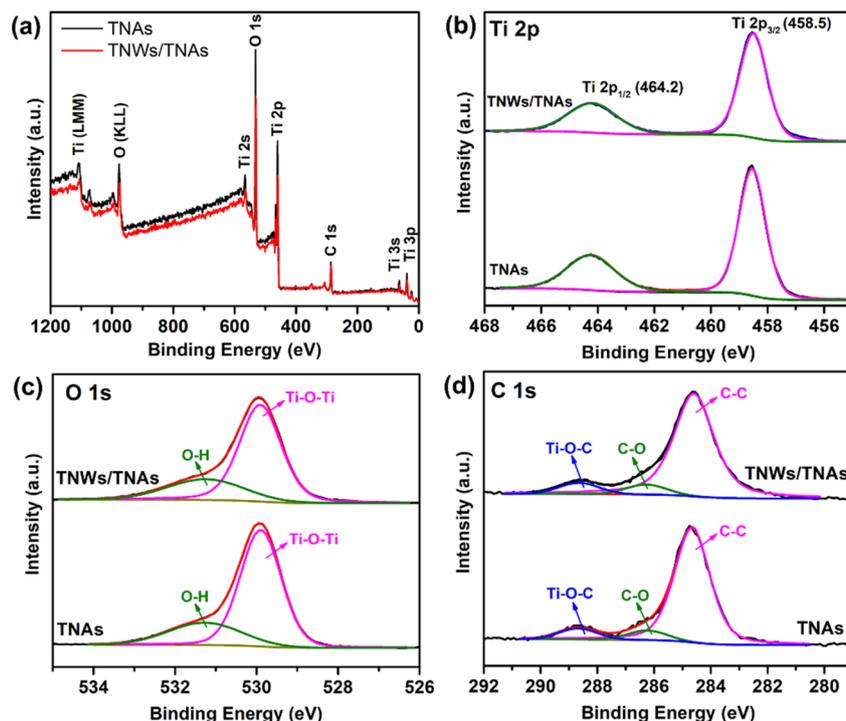**Fig. 4** TEM images of (a) TNAs and (b) TNWs/TNAs.

Fig. 5 (a) XPS survey spectra of TNAs and TNWs/TNAs. XPS spectra of the two TiO$_2$ nanomaterials in the (b) Ti 2p, (c) O 1s, and (d) C 1s regions.

compositional result is reasonable and consistent with the observed TiO$_2$ crystal phase from the XRD result.

Fig. 4 presents TEM images of TiO$_2$ nanotube arrays (TNAs) and TiO$_2$ nanowire/nanotube arrays (TNWs/TNAs). In Fig. 4(a), a segment of the TNA structure reveals a tube diameter of approximately 100 nm, a wall thickness of about 15 nm, and lattice fringes with a d-spacing of 0.35 nm, corresponding to the (101) planes of TiO$_2$. Meanwhile, Fig. 4(b) illustrates the mixed structure of TNWs/TNAs, where TiO$_2$ nanotubes coexist with nanowires. A segment of the TiO$_2$ nanowire also displays lattice fringes with a d-spacing of 0.35 nm, indicative of the (101) planes. These observations are consistent with the (101)-preferred orientation identified in the XRD results, further

validating the crystallographic structure of the synthesized TiO$_2$ nanostructured films.

The surface composition and chemical states of TNAs and TNWs/TNAs were analysed using XPS (Fig. 5). The wide-scan XPS spectra clearly reveal the presence of C 1s, Ti 2p, and O 1s peaks for both TNAs and TNWs/TNAs. Fig. 5(b) shows the Ti 2p spectra, with Ti 2p$_{1/2}$ and Ti 2p$_{3/2}$ peaks observed at 464.2 eV and 458.5 eV, respectively, indicating the Ti^{4+} oxidation state typical of TiO$_2$. Additionally, the O 1s spectrum displays an asymmetrical peak with a tail extending towards higher energy (Fig. 5(c)). Thus, this O 1s spectrum was deconvoluted into two component peaks at 529.9 eV of Ti–O–Ti bonds (lattice oxygen) and 531.3 eV of O–H bonds (Fig. 5(c)), agreeing with the XPS
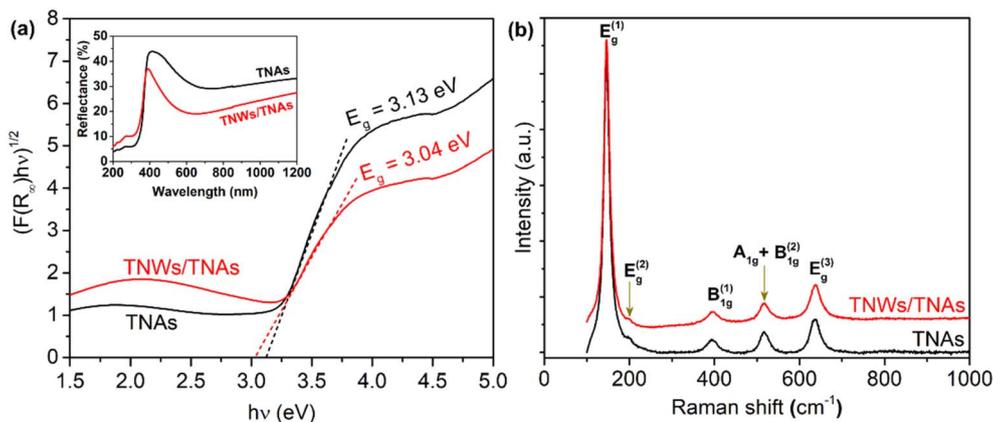

Fig. 6 (a) The plot of the transformed Kubelka–Munk function *versus* absorbed photon energy for TNAs and TNWs/TNAs; the extrapolated lines and corresponding optical bandgaps of TNAs and TNWs are depicted; the inset displays the reflectance spectra of TNAs and TNWs/TNAs. (b) Raman spectra of TNAs and TNWs/TNAs.

result of TiO$_2$ nanoparticles.[48] In Fig. 5(d), the C 1s XPS spectra for TNAs and TNWs/TNAs were deconvoluted into three peaks at 284.6, 286.3, and 288.6 eV, corresponding to C–C, C–O, and Ti–O–C bonds, respectively.[48] These XPS results align with previous studies on TiO$_2$ nanoparticles[48] and TNWs/TNAs.[20]

From the DRS spectra in Fig. 6(a), the optical band gaps of the TNA and TNW/TNA films were determined by extrapolating the linear portion of the $[F(R_\infty)h\nu]^{0.5}$ plot, based on an indirect transition. The optical band gaps were found to be 3.13 eV for TNAs and 3.04 eV for TNWs/TNAs (Fig. 6(a)), consistent with the well-established band gap of approximately 3.1 eV for anatase TiO$_2$[49] and 3.1–3.22 eV for TiO$_2$ materials.[50,51] Notably, TNWs/TNAs exhibited lower reflectance compared to TNAs, likely due to their rougher surface (as shown in the inset of Fig. 6(a) and in Fig. 3(b)). This occurs because smooth surfaces reflect light more uniformly, whereas rough or textured surfaces scatter light in multiple directions, resulting in a reduced overall reflectance.

In Fig. 6(b), characteristic peaks observed at 146 cm^{-1} (E$_g^{(1)}$), 200 cm^{-1} (E$_g^{(2)}$), 397 cm^{-1} (B$_{1g}^{(1)}$), 517 cm^{-1} (A$_{1g}$ + B$_{1g}^{(2)}$), and 638 cm^{-1} (E$_g^{(3)}$) align with the vibrational modes of anatase TiO$_2$.[22,52,53] The E$_g$ modes correspond to the symmetric stretching vibrations of Ti–O bonds, while B$_{1g}$ and A$_{1g}$ modes represent symmetric and antisymmetric bending motions of O–Ti–O, respectively.[52–54] The presence of these identification Raman characteristic peaks of anatase TiO$_2$ and the absence of any prominent peaks corresponding to the rutile phase[54] confirm that both TNAs and TNWs/TNAs retain a well-crystallized anatase structure that is advantageous for high photocatalytic activity and efficient electron transport.

3.6. Photocatalytic degradation of pesticide residues in agriculture water samples by TiO$_2$ nanomaterials

Fig. 7(a) shows the photocatalytic degradation of carbaryl by using TNAs and TNWs/TNAs under UV-vis irradiation. The concentration of carbaryl decreases over time following an exponential decay, as described by the equation $C_t = C_0 \times e^{-kt}$, where C_0 is the initial concentration (ng mL^{-1}), C_t is the pesticide concentration at time t (ng mL^{-1}), and k is the reaction rate constant (min^{-1}). The C_t/C_0 vs. t curves for other pesticides (MTC, DZN, CLO, and CYPER) are similar to the demonstrated carbaryl one. Fig. 7(b) summarizes the obtained k values of TNAs and TNWs/TNAs in photocatalytic degradation of the five pesticides. The k values varied in the range of 2.5×10^{-2}–44.8×10^{-2} min^{-1}, depending on the pesticide with the order of k values being $k_{CLO} < k_{CBR} < k_{DZN} < k_{MTC} < k_{CYPER}$. Additionally, TNWs/TNAs consistently show higher photocatalytic activity than TNAs, likely due to their larger surface area and thicker film.

Chlorpyrifos (CLO) is the most challenging drug to decompose among the ones tested. This is because of the structural characteristic of CLO, with few conjugated double bonds. CLO has absorption peaks at 229 nm and 290 nm in the UV-vis spectrum, and it is relatively stable to UV-C light.[55,56] A study on Cu-doped TiO$_2$/GO composite nanoparticles found that chlorpyrifos removal efficiencies were 91.4% under UV light and 78.25% under visible light, with respective rate constants of 3.01×10^{-2} min^{-1} and 1.77×10^{-2} min^{-1} for an irradiation time of 80 minutes.[57] In this study, complete removal of CLO was achieved after 25 minutes under UV-vis irradiation, with rate constants of 2.46×10^{-2} min^{-1} for TNAs and 2.59×10^{-2} min^{-1} for TNW/TNA materials. However, making a fair comparison of k values across different studies is challenging due to variations in experimental conditions. The complete removal time of the analyte depends significantly on its initial concentration. Additionally, factors such as the type of light source, solution volume, and the quantity of nanomaterials used can further influence the results, making direct comparison difficult. Nevertheless, the consistently low rate constants in both studies suggest the difficulty in decomposing CLO. The similarity in the rate constants implies that alterations in TiO$_2$ morphology hold promise for effectively enhancing its performance, as does
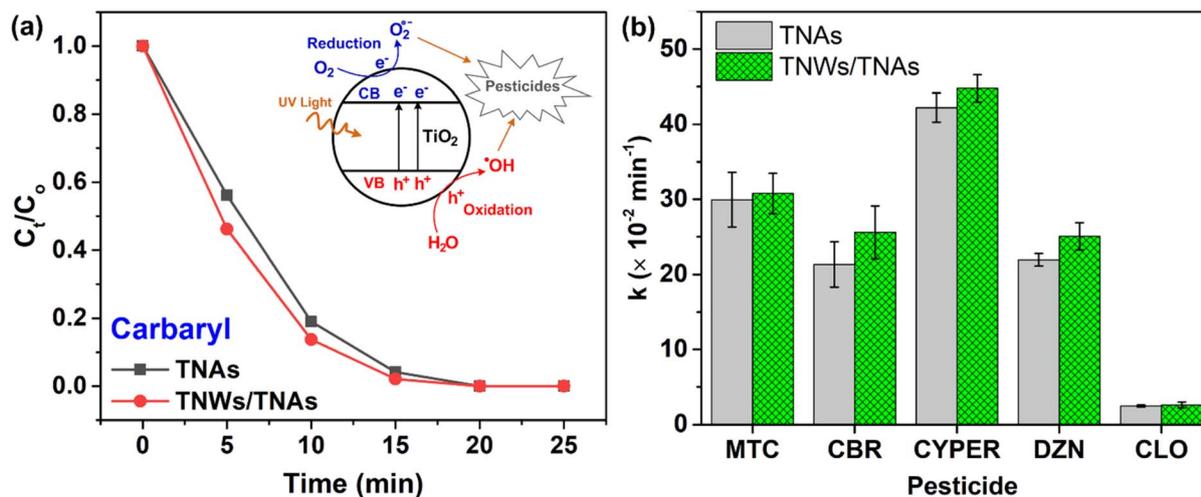

Fig. 7 (a) Photocatalytic degradation of carbaryl using TNAs and TNWs/TNAs under 96 mW cm^{-2} UV-vis irradiation. (b) The photocatalytic reaction rate constants of TNAs and TNWs/TNAs in degradation of the five pesticides. Abbreviations: MTC: methiocarb; CBR: carbaryl; CYPER: cypermethrin; DZN: diazinon; CLO: chlorpyrifos.

doping TiO_2 with other materials. In this research, the material was synthesized by permanently affixing it to a titanium plate. This approach facilitates a higher recovery compared to the material in nanopowder form, expands the potential for material reuse, and mitigates the risk of secondary environmental pollution.

The rate constant values for carbaryl decomposition with TNAs and TNW/TNAs are 21.32×10^{-2} min^{-1} and 25.60×10^{-2} min^{-1}, respectively, nearly ten times higher than the value obtained using TiO_2-coated glass-fiber filters, 2.2×10^{-2}–2.5×10^{-2} min^{-1}.[58] While some studies have shown degradation of methiocarb using electro-Fenton processes[59] and electrochemical oxidation,[60] none have employed TiO_2 for methiocarb degradation. TiO_2, in powder form or combined with other materials, has been used to degrade cypermethrin[61–64] and diazinon,[65–70] but no studies have utilized TiO_2 nanotubes (TNAs) or nanowires on TiO_2 nanotubes (TNWs/TNAs) for the elimination of these pesticides. To the best of our knowledge, this is the first time TNAs and TNWs/TNAs have been used to simultaneously eliminate five pesticides from environmental samples.

The inset in Fig. 7(a) illustrates the schematic mechanism of the photocatalytic degradation of pesticides by TiO_2. Under UV illumination (photon energy > E_g ~3.2 eV for TiO_2), energetic electrons are injected into the conduction band, while holes are created in the valence band. Reduction and oxidation reactions then occur in the treated solution, generating substantial amounts of reactive oxygen species, such as superoxide radicals $(O_2^{\bullet-})$ and hydroxyl radicals $(^{\bullet}OH)$. These reactive oxygen species facilitate the mineralization and transformation of toxic pesticides.[29]

The photocatalytic performance of TiO_2 nanomaterials is strongly influenced by their microstructural properties, which play a crucial role in determining their efficacy in the degradation of pesticide contaminants. TiO_2 nanotube arrays, with their unique 2D porous structure, provide an extended surface area that facilitates greater adsorption of pesticide molecules. The increased surface area also enhances the formation of reactive oxygen species, which are essential for breaking down organic pollutants. Furthermore, the ordered arrangement of nanotubes enables better electron–hole separation, which is key to enhancing the photocatalytic efficiency. The high aspect ratio and long-range order of the nanotubes promote efficient charge transport, thus reducing the recombination of electron–hole pairs and ensuring sustained photocatalytic activity.[71] These structural advantages make TiO_2 nanotube arrays highly effective in degrading pesticides, as they maximize the exposure of active sites and facilitate faster reaction rates under UV illumination.

The high surface-to-volume ratio of nanowires increases the adsorption capacity for pesticide molecules, allowing for efficient degradation. Additionally, the nanowires' electrical conductivity improves the transfer of photogenerated electrons to the surface,[72] where they can participate in redox reactions that lead to the formation of reactive species. As a result, TiO_2 nanowires exhibit superior photocatalytic activity compared to conventional TiO_2 films, particularly when applied to environmental remediation of pesticide-contaminated water.

The synergetic effect of TiO_2 nanowires (TNWs) and TiO_2 nanotube arrays (TNAs) arises from their complementary structural and functional advantages, leading to enhanced performance in photocatalytic applications.[20,22,28] The nanowires on nanotube arrays (TNWs/TNAs) architecture significantly increases the available surface area, providing more active sites for catalysis, adsorption, and charge transfer. The extended nanowires improve light harvesting by enhancing light scattering and trapping, which boosts photon absorption and makes the structure more effective in photodegradation of pollutants/contaminants.[20,22,28] Together, these synergistic
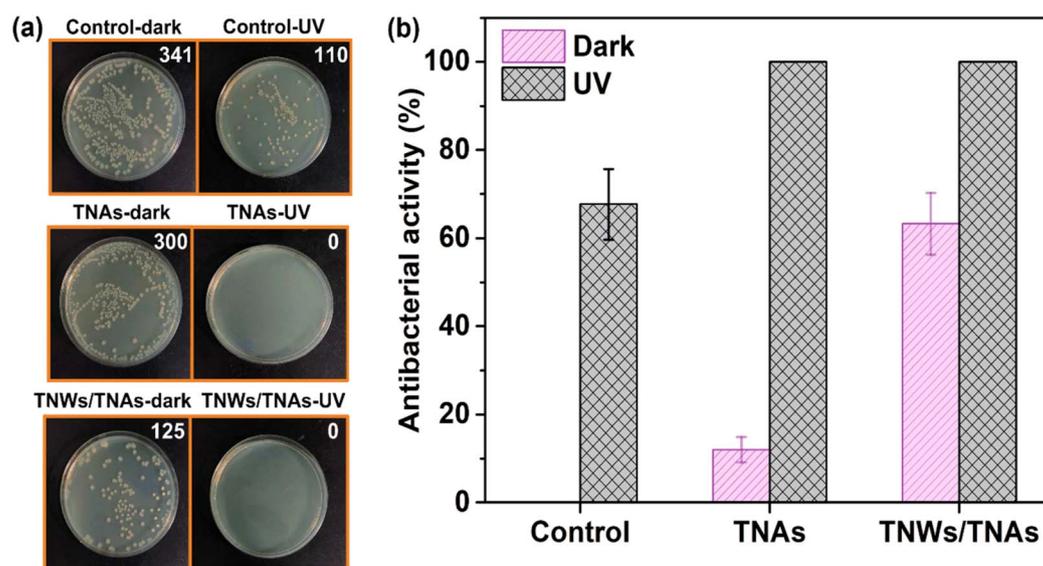

Fig. 8   (a) Images of *E. coli* after 22 hours of incubation for control, TNA, and TNW/TNA samples, both under dark conditions and 10 minutes of UV irradiation (6.3 mW cm^{-2}). (b) Antibacterial activity (%) of the respective samples.

effects make TNWs/TNAs a superior material design for environmental remediation.

The TNA-based films, fabricated *via* anodic oxidation, showed only a slight decrease in anticancer drug degradation efficiency after five cycles of reuse.[22] This suggests that TNWs/TNAs, synthesized under similar anodic oxidation conditions and with comparable film thickness, could also exhibit excellent reusability.

3.7. Antimicrobial activities of TNAs and TNWs/TNAs nanostructured films

Fig. 8 demonstrates the antibacterial efficacy of both TNAs and TNWs/TNAs, with the number of bacterial colonies indicated in the upper right corner of each experimental sample. The results show that under light exposure, TNAs and TNWs/TNAs achieve a 100% antibacterial rate, significantly outperforming the 68% efficacy of UV light at 253 nm, 32 W. This enhanced antibacterial activity under light is attributed to the generation of photooxidative radicals by TiO_2, which rapidly disrupts the bacterial cell wall and membrane, penetrates the cell, and inhibits essential biological processes such as the respiratory chain, DNA synthesis, and assimilation and transport of iron and inorganic phosphate. These combined effects substantially enhance the antibacterial performance.[30]

Interestingly, even in the absence of light, TNAs demonstrate a modest antibacterial activity of approximately 12%, which increases significantly to 63% in the case of TNWs/TNAs, approaching the efficacy of UV light. This increased effectiveness can be ascribed to TiO_2's ability to damage the bacterial cell wall's outer membrane through electrostatic interactions or direct contact between the nanomaterial and the cell wall.[73] Moreover, TiO_2 inhibits bacterial aggregation and biofilm formation—two critical factors in pathogenicity.[74] However, the antibacterial effect of TiO_2 without light exposure depends heavily on its surface characteristics. It is well established that the antibacterial activity of TiO_2 is influenced by its size, shape, and surface chemistry, which significantly impact its photocatalytic properties and interaction time with bacteria.[75–77]

In our study, TNWs/TNAs exhibited superior antibacterial efficacy compared to TNAs alone, likely due to their higher surface area and enhanced photocatalytic properties. In contrast, other TiO_2 forms, such as free-standing bundles of TiO_2 nanotubes and commercial TiO_2 particles, have been reported to be ineffective in inhibiting bacterial growth under dark conditions.[31,32,78] Fig. 9 presents the antibacterial activity of TNAs and TNWs/TNAs nanostructured membranes under UV light irradiation and dark conditions, while Table 1 provides a comparison of their antibacterial performance with other TiO_2-based nanomaterials. The enhanced antibacterial performance of TNWs/TNAs over TNAs alone in this study is likely due to the material's surface morphology, which contributes to the improved antibacterial efficacy.

Beyond their role in photocatalytic pesticide degradation and antimicrobial activity, the TiO_2 nanomaterials (TNAs and TNWs/TNAs) offer diverse applications due to their high surface area, charge transport efficiency, and photocatalytic properties. They are effective in water and wastewater treatment by degrading organic pollutants, reducing heavy metals, and disinfecting pathogens.[31,81,82] In air purification, they help remove volatile organic compounds and toxic gases.[83] Their energy applications include dye-sensitized solar cells and photocatalytic hydrogen production.[84,85] Additionally, they serve as antibacterial coatings in medical devices and as catalysts in industrial processes, including oxidation reactions and CO_2 reduction.[86,87]

While the experimental results highlight the excellent photocatalytic degradation of pesticides and antibacterial properties of TNAs and TNWs/TNAs against *E. coli* under laboratory conditions, their practical application in agricultural water treatment presents several challenges. Key factors that require further investigation include the scalability of photocatalytic reactors to ensure uniform light exposure, the stability of light conditions under varying environmental factors, and the impact of impurities or complex matrices on real agricultural wastewater. Future research should focus on optimizing TiO_2 nanostructures for integration into large-scale reactor systems, enhancing their stability in mixed-contaminant environments and utilizing solar energy for cost-effective operation. Additionally, addressing potential secondary pollution, such as the
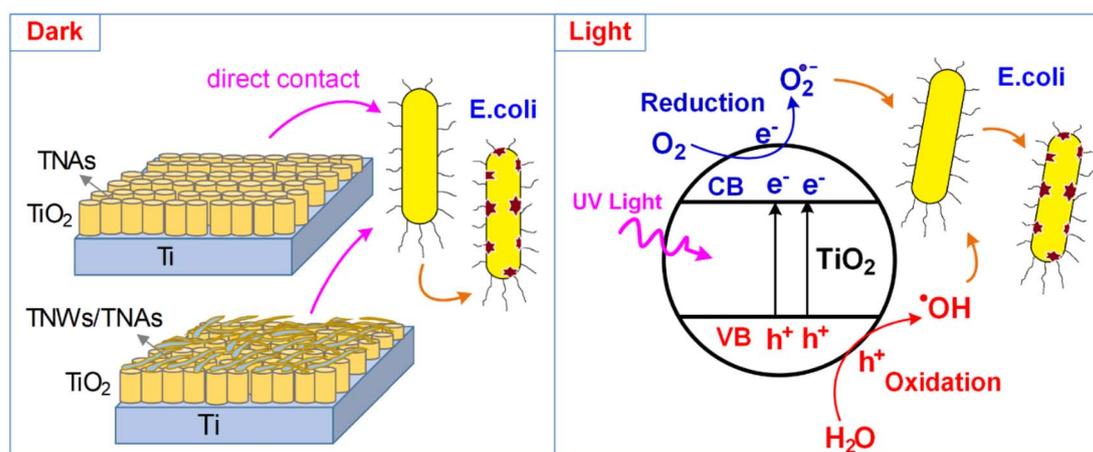

Fig. 9 The mechanism of antibacterial activity of TNAs and TNWs/TNAs under UV irradiation and in a dark environment.

Paper

Table 1 Sterilization efficacy of TNAs, TNWs/TNAs, and other TiO$_2$-based photocatalytic nanomaterials against *E. coli* as reported in the literature

Catalyst	Light source	Irradiation time	Antibacterial activity (%)	Reference
TiO$_2$ nanopowder	None	None	0	31
TiO$_2$ nanopowder	None	None	0	32
La-doped TiO$_2$ nanopowder	None	None	0	79
TNAs	None	None	12	This study
TNWs/TNAs	None	None	63	This study
TiO$_2$ P25	UV-A/-B light	24 h	0	78
TiO$_2$/Ag nanoparticles	None	None	95	80
Free-standing bundles of TiO$_2$ nanotubes	UV-A/-B light	24 h	97.53	78
La-doped TiO$_2$ nanopowder	UV 365 nm, 8 W	15 min	100	79
TNAs	UV 253 nm, 32 W	10 min	100	This study
TNWs/TNAs	UV 253 nm, 32 W	10 min	100	This study

unintentional release of nanomaterials, and improving the reusability of photocatalysts will be critical for sustainable deployment. By tackling these challenges, future studies can bridge the gap between laboratory findings and real-world applications, advancing the use of TiO$_2$-based photocatalysis for agricultural water treatment and environmental sustainability.

4. Conclusions

We developed a simple, selective, sensitive, accurate, and reproducible UPLC-MS/MS method for the quantitative analysis of five pesticide residues in agricultural water samples from the Mekong Delta region, Vietnam. The method was fully validated and met all the established criteria. Upon testing 40 water samples from rice-growing areas in Can Tho City and Hau Giang Province, we detected a significant occurrence and high frequency of pesticide residues in surface water, with chlorpyrifos exhibiting the highest contamination rate (32.5%, average concentration of 1.7–10.9 ng mL^{-1}). Four other pesticides of cypermethrin (2.6–9.4 ng mL^{-1}), carbaryl (1.3–14.3 ng mL^{-1}), methiocarb (4.1–7.7 ng mL^{-1}), and diazinon (2.8–10.5 ng mL^{-1}) were also detected. Additionally, we investigated the photocatalytic degradation of these pesticide residues using TiO$_2$ nanomaterials (TNAs and TNWs/TNAs), both of which proved to be effective photocatalysts. In particular, the nanocatalysts achieved up to 99% pesticide degradation within 25 minutes under UV-vis irradiation (∼96 mW cm^{-2}), with TNWs/TNAs showing superior performance owing to their morphology characteristic and the larger surface area compared to TNAs. The study also highlighted the remarkable antibacterial efficacy of TNAs and TNWs/TNAs, achieving 100% antibacterial rate after just 10 minutes of UV-vis light exposure (6.3 mW cm^{-2}). Notably, even in the absence of light, TNWs/TNAs exhibited greater antibacterial activity than TNAs, suggesting TNWs/TNAs as an effective antibacterial nanostructured film.

Data availability

The data supporting this article have been included as part of the ESI.†

Author contributions

Phuoc Huu Le: conceptualization, methodology, investigation, formal analysis, writing – review & editing, supervision, funding acquisition. Thao Phuong Huynh: methodology, visualization, writing – original draft. Loc Tan Nguy: investigation, formal analysis, data curation. Teng-Ping Chu: investigation, formal analysis. Ngo Ngoc Uyen: investigation, data curation. Tho Chau Minh Vinh Do: resources, conceptualization, methodology, supervision, writing – review & editing.

Conflicts of interest

There are no conflicts to declare.

Acknowledgements

References

1 M. A. Hassaan and A. El Nemr, *Egypt. J. Aquat. Res.*, 2020, **46**, 207–220.

2 D. V. Binh, S. A. Kantoush, M. Saber, N. P. Mai, S. Maskey, D. T. Phong and T. Sumi, *J. Hydrol.: Reg. Stud.*, 2020, **32**, 100742.

3 P. V. Toan, Z. Sebesvari, M. Blasing, I. Rosendahl and F. G. Renaud, *Sci. Total Environ.*, 2013, **452–453**, 28–39.

4 N. D. Chau, Z. Sebesvari, W. Amelung and F. G. Renaud, *Environ. Sci. Pollut. Res. Int.*, 2015, **22**, 9042–9058.

5 I. El-Nahhal and Y. El-Nahhal, *J. Environ. Manage.*, 2021, **299**, 113611.

6 C. Olisah, O. O. Okoh and A. I. Okoh, *Heliyon*, 2020, **6**, e03518.

7   J. da Silva Sousa, H. O. do Nascimento, H. de Oliveira Gomes and R. F. do Nascimento, *Microchem. J.*, 2021, **168**, 106359.

8   J. Chen, C. Wang, X. Huang, R. Wan, Z. Zhu, G. Sun, X. Wang, H. Chen, L. Han, L. Li, H. Li and Z. Chi, *Adv. Funct. Mater.*, 2025, 2423643, DOI: 10.1002/adfm.202423643.

9   C. Campanale, C. Massarelli, D. Losacco, D. Bisaccia, M. Triozzi and V. F. Uricchio, *TrAC, Trends Anal. Chem.*, 2021, **144**, 116423.

10 J. Lundqvist, C. von Brömssen, A. K. Rosenmai, Å. Ohlsson, T. Le Godec, O. Jonsson, J. Kreuger and A. Oskarsson, *Environ. Sci. Eur.*, 2019, **31**, 53.

11 M. Syafrudin, R. A. Kristanti, A. Yuniarto, T. Hadibarata, J. Rhee, W. A. Al-Onazi, T. S. Algarni, A. H. Almarri and A. M. Al-Mohaimeed, *Int. J. Environ. Res. Public Health*, 2021, **18**, 468.

12 T. Wang, M. Zhong, M. Lu, J. Huang, L. Blaney and G. Yu, *Anal. Methods*, 2021, **13**, 3160–3171.

13 M. Nehra, N. Dilbaghi, G. Marrazza, A. Kaushik, C. Sonne, K. H. Kim and S. Kumar, *J. Hazard. Mater.*, 2021, **401**, 123369.

14 H. Dong, L. Xu, Y. Mao, Y. Wang, S. Duan, J. Lian, J. Li, J. Yu and Z. Qiang, *J. Hazard. Mater.*, 2021, **403**, 123986.

15 T. K. Patle, R. Kurrey, K. Dewangan and K. Shrivas, in *Multifunctional Hybrid Nanomaterials for Sustainable Agri-Food and Ecosystems*, Elsevier, 2020, pp. 241–254, DOI: 10.1016/b978-0-12-821354-4.00010-8.

16 R. Fiorenza, A. Di Mauro, M. Cantarella, C. Iaria, E. M. Scalisi, M. V. Brundo, A. Gulino, L. Spitaleri, G. Nicotra, S. Dattilo, S. C. Carroccio, V. Privitera and G. Impellizzeri, *Chem. Eng. J.*, 2020, **379**, 122309.

17 W. Xu, W. Fu, X. Meng, M. Tang, C. Huang, Y. Sun and Y. Dai, *Nanoscale*, 2021, **13**, 20564–20575.

18 Q. Guo, C. Zhou, Z. Ma and X. Yang, *Adv. Mater.*, 2019, **31**, e1901997.

19 P. H. Le, L. T. Hieu, T. N. Lam, N. T. N. Hang, N. V. Truong, L. T. C. Tuyen, P. T. Phong and J. Leu, *Micromachines*, 2018, **9**, 618.

20 N. N. Uyen, L. T. C. Tuyen, L. T. Hieu, T. T. T. Nguyen, H. P. Thao, T. C. M. V. Do, K. T. Nguyen, N. T. N. Hang, S.-R. Jian, L. A. Tu, P. H. Le and C.-W. Luo, *Coatings*, 2022, **12**, 1957.

21 T. Do, D. Q. Nguyen, K. T. Nguyen and P. H. Le, *Materials*, 2019, **12**, 2434.

22 T. P. Huynh, T. C. M. V. Do and P. H. Le, *ACS Appl. Nano Mater.*, 2024, **7**, 20012–20023.

23 M.-Y. Hsu, H.-L. Hsu and J. Leu, *J. Electrochem. Soc.*, 2012, **159**, H722–H727.

24 S. Sayegh, F. Tanos, A. Nada, G. Lesage, F. Zaviska, E. Petit, V. Rouessac, I. Iatsunskyi, E. Coy, R. Viter, D. Damberga, M. Weber, A. Razzouk, J. Stephan and M. Bechelany, *Dalton Trans.*, 2022, **51**, 2674–2695.

25 M. Moura, V. E. Lima, A. A. M. Neto, A. L. A. Lucena, D. C. Napoleao and M. Duarte, *Water Sci. Technol.*, 2021, **83**, 863–876.

26 N. Ahmadpour, M. H. Sayadi, S. Sobhani and M. Hajiani, *J. Environ. Manage.*, 2020, **271**, 110964.

27 Z. Li, H. Bian, X. Xiao, J. Shen, C. Zhao, J. Lu and Y. Y. Li, *ACS Appl. Nano Mater.*, 2019, **2**, 7372–7378.

28 T. C. M. V. Do, D. Q. Nguyen, T. D. Nguyen and P. H. Le, *Catalysts*, 2020, **10**, 356.

29 M. Hadei, A. Mesdaghinia, R. Nabizadeh, A. H. Mahvi, S. Rabbani and K. Naddafi, *Environ. Sci. Pollut. Res. Int.*, 2021, **28**, 13055–13071.

30 D. Carol López de, C. Matias Guerrero, B. M. Fernanda, S. Camilo and G. Maria José, in *Antimicrobial Resistance*, ed. M. Mihai, L. Swee Hua Erin, L. Kok-Song and C. Romeo-Teodor, IntechOpen, Rijeka, 2020, ch. 5, p. 90891, DOI: 10.5772/intechopen.90891.

31 A. Petica, A. Florea, C. Gaidau, D. Balan and L. Anicai, *J. Mater. Res. Technol.*, 2019, **8**, 41–53.

32 A. Steinbach, D. Svab, L. Korosi, M. Kerenyi, J. Kun, P. Urban, T. Palkovics, T. Kovacs and S. Gyorgy, *Heliyon*, 2024, **10**, e33562.

33 T. Munir, A. Mahmood, N. Abbas, A. Sohail, Y. Khan, S. Rasheed and I. Ali, *ACS Omega*, 2024, **9**, 34841–34847.

34 B. Xue, A. Hou, Y. Du, Y. Qi, H. Jiang, H. Zhou, Z. Zhou and H. Chen, *Surf. Interfaces*, 2023, **39**, 102996.

35 C. López de Dicastillo, C. Patiño, M. J. Galotto, J. L. Palma, D. Alburquenque and J. Escrig, *Nanomaterials*, 2018, **8**, 128.

36 R. C. de Oliveira, C. C. de Foggi, M. M. Teixeira, M. D. P. da Silva, M. Assis, E. M. Francisco, B. N. A. d. S. Pimentel, P. F. d. S. Pereira, C. E. Vergani, A. L. Machado, J. Andres, L. Gracia and E. Longo, *ACS Appl. Mater. Interfaces*, 2017, **9**, 11472–11481.

37 Z. He, Q. Cai, H. Fang, G. Situ, J. Qiu, S. Song and J. Chen, *J. Environ. Sci.*, 2013, **25**, 2460–2468.

38 G. Vimbela, S. M. Ngo, C. Fraze, L. Yang and D. A. Stout, *Int. J. Nanomed.*, 2017, **12**, 3941–3965.

39 E. Widyastuti, C.-T. Chiu, J.-L. Hsu and Y. Chieh Lee, *Arabian J. Chem.*, 2023, **16**, 105010.

40 L. S. Daniel, M. T. Joseph, V. Uahengo and M. Hedimbi, *Adv. Mater. Interfaces*, 2024, **11**, 2400035.

41 J. Paniagua-Méndez, S. L. Ramírez-Sandoval, E. Reyes-Uribe and M. E. Contreras-García, *Ceram. Int.*, 2024, **50**, 34421–34430.

42 R. P. Carneiro, F. A. S. Oliveira, F. D. Madureira, G. Silva, W. R. de Souza and R. P. Lopes, *Food Control*, 2013, **33**, 413–423.

43 H. Imamoglu and E. Oktem Olgun, *J. Anal. Methods Chem.*, 2016, **2016**, 2170165.

44 B. Garlito, M. Ibanez, T. Portoles, R. Serrano, H. Amlund, A. K. Lundebye, M. Sanden, M. H. G. Berntssen and F. Hernandez, *Anal. Bioanal. Chem.*, 2019, **411**, 7281–7291.

45 D. Shin, J. Kim and H.-S. Kang, *Food Control*, 2021, **120**, 107552.

46 K. Zheng, X. Wu, J. Chen, J. Chen, W. Lian, J. Su and L. Shi, *Molecules*, 2022, **27**, 8674.

47 M. Masis-Mora, W. Beita-Sandi, J. Rodriguez-Yanez and C. E. Rodriguez-Rodriguez, *J. Chromatogr. B: Anal. Technol. Biomed. Life Sci.*, 2020, **1156**, 122296.

48 K. Jia, Y. Wang, Q. Pan, B. Zhong, Y. Luo, G. Cui, X. Guo and X. Sun, *Nanoscale Adv.*, 2019, **1**, 961–964.

49 Z. Li, S. Wang, J. Wu and W. Zhou, *Renewable Sustainable Energy Rev.*, 2022, **156**, 111980.

50 P. Makula, M. Pacia and W. Macyk, *J. Phys. Chem. Lett.*, 2018, **9**, 6814–6817.

51 H. Yaghoubi, Z. Li, Y. Chen, H. T. Ngo, V. R. Bhethanabotla, B. Joseph, S. Ma, R. Schlaf and A. Takshi, *ACS Catal.*, 2014, **5**, 327–335.

52 B. Taudul, F. Tielens and M. Calatayud, *Nanomaterials*, 2023, **13**, 1856.

53 T. Ohsaka, F. Izumi and Y. Fujiki, *J. Raman Spectrosc.*, 1978, **7**, 321–324.

54 T. Mazza, E. Barborini, P. Piseri, P. Milani, D. Cattaneo, A. Li Bassi, C. E. Bottani and C. Ducati, *Phys. Rev. B: Condens. Matter Mater. Phys.*, 2007, **75**, 045416.

55 J. Ho, R. Prosser, M. Hasani, H. Chen, B. Skanes, W. D. Lubitz and K. Warriner, *Food Control*, 2020, **109**, 106920.

56 G. Kanade, D. Tripathi, S. Lari and K. Gandhi, *J. Water Reuse Desalin.*, 2016, **6**, 195–203.

57 H. Esfandian, S. Mirzaei, A. S. Chari, R. A. Ghadi and I. H. Moqadam, *Mater. Sci. Eng., B*, 2024, **305**, 117385.

58 J. Jampawal, S. Supothina and P. Chuaybamroong, *Environ. Sci. Pollut. Res.*, 2022, **29**, 88027–88040.

59 F. Souiad, A. S. Rodrigues, A. Lopes, L. Ciriaco, M. J. Pacheco, Y. Bendaoud-Boulahlib and A. Fernandes, *Molecules*, 2020, **25**, 5893.

60 A. Fernandes, C. Pereira, S. Coelho, C. Ferraz, A. C. Sousa, M. R. Pastorinho, M. J. Pacheco, L. Ciríaco and A. Lopes, *Appl. Sci.*, 2020, **10**, 7435.

61 M. Tran Thi Ngoc, D.-T. Van-Pham, Q. Tran Thi Bich, M. Ngo Truong Ngoc, D. Ta Ngoc and T. Doan Van Hong, *Vietnam J. Catal. Adsorpt.*, 2022, **11**, 22–27.

62 R. A. Solano Pizarro and A. P. Herrera Barros, *Adv. Compos. Lett.*, 2020, **29**, 1–13.

63 M. Nurdin, M. Maulidiyah, L. O. A. Salim, M. Z. Muzakkar and A. A. Umar, *Microchem. J.*, 2019, **145**, 756–761.

64 A. C. Affam and M. Chaudhuri, *J. Environ. Manage.*, 2013, **130**, 160–165.

65 R. K. S. Mhemid, L. I. Saeed and R. N. Mohammed, *Int. J. Environ. Sci. Technol.*, 2024, **21**, 329–340.

66 S. Amiri and M. Anbia, *Mater. Res. Bull.*, 2023, **165**, 112289.

67 M. A. I. Molla, M. Furukawa, I. Tateishi, H. Katsumata and S. Kaneco, *Environ. Technol.*, 2020, **41**, 3524–3533.

68 N. M. Phuong, N. C. Chu, D. Van Thuan, M. N. Ha, N. T. Hanh, H. D. T. Viet, N. T. Minh Thu, P. Van Quan and N. T. Thanh Truc, *J. Chem.*, 2019, **2019**, 1–7.

69 S. Tabasideh, A. Maleki, B. Shahmoradi, E. Ghahremani and G. McKay, *Sep. Purif. Technol.*, 2017, **189**, 186–192.

70 A. Jonidi-Jafari, M. Shirzad-Siboni, J.-K. Yang, M. Naimi-Joubani and M. Farrokhi, *J. Taiwan Inst. Chem. Eng.*, 2015, **50**, 100–107.

71 C. Allard, L. Alvarez, J. L. Bantignies, N. Bendiab, S. Cambre, S. Campidelli, J. A. Fagan, E. Flahaut, B. Flavel, F. Fossard, E. Gaufres, S. Heeg, J. S. Lauret, A. Loiseau, J. B. Marceau, R. Martel, L. Marty, T. Pichler, C. Voisin, S. Reich, A. Setaro, L. Shi and W. Wenseleers, *Chem. Soc. Rev.*, 2024, **53**, 8457–8512.

72 M. Zimbone, S. Battiato, L. Calcagno, G. Pezzotti Escobar, G. Pellegrino, S. Mirabella, F. Giuffrida and G. Impellizzeri, *J. Mater. Sci.*, 2024, **59**, 17831–17845.

73 H. H. Bahjat, R. A. Ismail, G. M. Sulaiman and M. S. Jabir, *J. Inorg. Organomet. Polym. Mater.*, 2021, **31**, 3649–3656.

74 A. Kubacka, C. Serrano, M. Ferrer, H. Lünsdorf, P. Bielecki, M. L. Cerrada, M. Fernández-García and M. Fernández-García, *Nano Lett.*, 2007, **7**, 2529–2534.

75 K. S. Khashan, G. M. Sulaiman, F. A. Abdulameer, S. Albukhaty, M. A. Ibrahem, T. Al-Muhimeed and A. A. AlObaid, *Appl. Sci.*, 2021, **11**, 4623.

76 E. Sanchez-Lopez, D. Gomes, G. Esteruelas, L. Bonilla, A. L. Lopez-Machado, R. Galindo, A. Cano, M. Espina, M. Ettcheto, A. Camins, A. M. Silva, A. Durazzo, A. Santini, M. L. Garcia and E. B. Souto, *Nanomaterials*, 2020, **10**, 292.

77 C. Han, N. Romero, S. Fischer, J. Dookran, A. Berger and A. L. Doiron, *Nanotechnol. Rev.*, 2017, **6**, 383–404.

78 J. Podporska-Carroll, E. Panaitescu, B. Quilty, L. Wang, L. Menon and S. C. Pillai, *Appl. Catal., B*, 2015, **176–177**, 70–75.

79 A. Stoyanova, H. Hitkova, N. Kaneva, A. Bachvarova-Nedelcheva, R. Iordanova and P. Marinovska, *Catalysts*, 2024, **14**, 469.

80 N. Nasab, M. Jalili and S. Farrokhpay, *J. Appl. Polym. Sci.*, 2017, **135**, 45913.

81 E. A. AbdulKareem, Z. H. Mahmoud and A. A. Khadom, *Case Stud. Chem. Environ. Eng.*, 2023, **8**, 100446.

82 M. H. Sosa Lissarrague, S. Alshehri, A. Alsalhi, V. L. Lassalle, I. López Corral and R. Rehman, *Adsorpt. Sci. Technol.*, 2023, **2023**, 2728305.

83 Z. Maeno, M. Nishitani, T. Saito, K. Sekiguchi, N. Kagi and N. Namiki, *Molecules*, 2024, **29**, 3819.

84 T. Ghani, M. Mujahid, M. Mehmood, G. Zhang and S. Naz, *J. Saudi Chem. Soc.*, 2019, **23**, 1231–1240.

85 R. Lucchetti, A. Siciliano, L. Clarizia, D. Russo, I. Di Somma, F. Di Natale, M. Guida, R. Andreozzi and R. Marotta, *Environ. Sci. Pollut. Res. Int.*, 2017, **24**, 5898–5907.

86 S. Jafari, B. Mahyad, H. Hashemzadeh, S. Janfaza, T. Gholikhani and L. Tayebi, *Int. J. Nanomed.*, 2020, **15**, 3447–3470.

87 Z. Yuan, X. Zhu, X. Gao, C. An, Z. Wang, C. Zuo, D. D. Dionysiou, H. He and Z. Jiang, *Environ. Sci. Ecotechnol.*, 2024, **20**, 100368.